Numerical Modeling of an In-vessel Flow Limiter Using an Immersed Boundary Approach

M. Belliard

6th European Conference on Computational Mechanics (ECCM 6)
7th European Conference on Computational Fluid Dynamics (ECFD 7)
1115 June 2018, Glasgow, UK

NUMERICAL MODELING OF AN IN-VESSEL FLOW LIMITER USING AN IMMERSED BOUNDARY APPROACH

MICHEL BELLIARD[1]

[1] CEA DEN/DER/SESI
Cadarache Bât. 1222 F-13108 Saint Paul-lez-Durance
michel.belliard@cea.fr, https://www.researchgate.net/profile/Michel_Belliard

Key words: PWR T-H system, In-vessel flow limiter, CFD, Immersed Boundary Methods

Abstract. This work is in the context of the mitigation of the consequences of a large-break loss of coolant accident in a Pressurized Water Reactor. To minimize the flow leaving the vessel and prevent or delay the uncovering of the core, CEA has devised a device, named in-vessel flow limiter, limiting the flow of fluid from the vessel to the break. The goal is to interfere as little as possible with the nominal operation flow and maximize the fluid retained in the event of this kind of accident.
In order to quickly perform a series of 3D-CFD simulations to optimize this device, it is imperative to have a simulation tool that provides sufficiently accurate results in a reasonable time. For this goal, an immersed boundary condition approach is retained. The solid obstacles constituted by the fins of the device are not extruded from the fluid domain, but included in the calculation domain itself. Their presence is considered by a first-order in space local Direct Forcing term using a penalty approach.
Through 3D/1D up-scaling of CFD global quantities, local pressure-drop coefficients, induced by the in-vessel flow limiter, can be provided to Thermal-Hydraulic system safety codes. It allows safety studies of the thermal-hydraulic system taking into account the in-vessel flow limiter presence in a more realistic way.

1 INTRODUCTION

The context of this work is set in the domain of Generation III nuclear power plants. There are the innovative designs that are under construction or still in design phase [1]. More specifically, we focused on the light-water Pressurized Water Reactors (PWRs), which are the main type of reactors built and exploited in France. Nowadays passive safety systems are more and more included in the nuclear-reactor safety strategy to mitigate design basis accidents. A passive safety system is a system that activates itself without the need of mechanical or electrical actuation.
At CEA, some studies on passive safety systems have been done in the past years, notably for the in-vessel flow limiter (hydraulic diode) patented by the CEA [2] designed to limit the amount of water lost during the short-term sequence of a Large-Break (LB) Loss Of

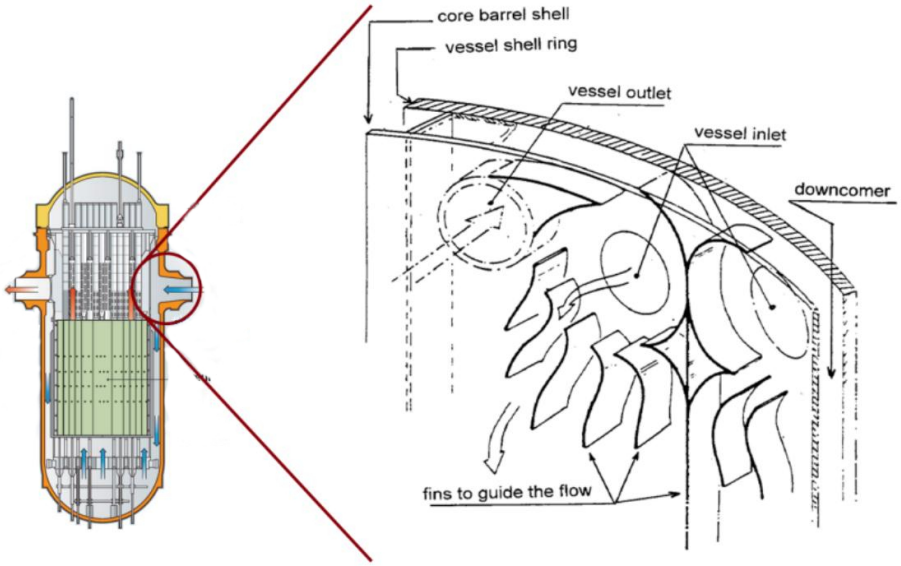

Figure 1: Scheme of in-vessel flow limiters (hydraulic diode) located between the cold legs and the downcomer [2].

Coolant Accident (LOCA), cf. Fig. 1. The goal is to interfere as little as possible with the nominal operation flow and maximize the fluid retained in the event of this kind of accident.

Numerical investigations of the benefices induced by the in-vessel flow limiter during LOCA transients have been done using thermal-hydraulic system safety codes. But, the relevance of these system-scale studies depends on the level of realism of the data introduced to take into account the hydraulic diodes. In order to take into account the large-scale effect of hydraulic diodes in safety-system studies, we need information coming from small-scale experimental or numerical experiments. For instance, results from 3D Computational Fluid Dynamic (CFD) simulations can be used to up-scale relevant characteristics as the global pressure drop induced by the hydraulic diode.

Moreover, CFD studies can be involved in the optimization process of the flow-limiter geometry to minimize the global pressure drop during nominal operations and to maximize it during a cold-leg LB-LOCA. This optimization process usually needed a big number of simulations. But, as many geometric scales are presented at the same time (typically several meters for the downcomer radial scale and one centimeter for the fin thickness), a CFD simulation of the two-phase flow inside the flow-limiter can be time consuming. Instead of this conventional approach (i.e. body-fitted approach), we are motivated by fictitious domain approach [3, 4] allowing a less precise but faster estimation of the pressure-drop coefficient. Following this way, we consider simulations over a full computational domain including the in-vessel flow-limiter fins and re-introduce their presence adding local external forces on the immersed boundaries. Moreover, a homogeneous relaxed equilibrium model of a liquid-vapour mixture [5] can be considered. For same space discretization, this kind of three-balance-equation model generally run faster than a six-balance-equation

model. Once a particular geometry exhibited as a good candidate, a reduced number of body-fitted CFD computations can be done to refine the design.

In this paper, we present a methodology concerning the design of a fast-running two-phase CFD model of the in-vessel flow-limiter device illustrated by CFD results. The numerical/experimental validation of this simulation tool is not the goal of this paper and only brief elements of validation are given here. The paper is structured as follow. The two-phase fluid CFD model and the first-order in space immersed boundary models are first presented in Sections 2 and 3. Then, the in-vessel flow limiter study, with the GENEPI code as CFD tool, is discussed in Section 4. Results provide a range of values that may be used in input of safety-system codes. Finally, some words concerning the perspectives of this work are given in Section 5.

2 The two-phase CFD model

The considered two-phase CFD model is the GENEPI one [6, 7], designed for the steam-generator two-phase flow steady-state 3D computations through the resolution of three balance equations for a water liquid/steam mixture. It is based on a homogeneous relaxed equilibrium model with thermodynamic equilibrium of the two phases. But closure laws take into account the liquid/steam momentum disequilibrium. This code incorporates the possibility to model thin no-penetration obstacles using Immersed Boundary Conditions (IBCs) [8].
Provided that the following assumptions hold: (i) surface tension, viscous and turbulent dissipation are neglected and pressure terms are neglected in the enthalpy balance equation, (ii) steam and liquid have same pressure, (iii) an eddy viscosity model is considered, one obtains for the mixture description of the two-phase flows the following mass, momentum and enthalpy balance equations:

$$\begin{aligned} \boldsymbol{\nabla}.\mathbf{G} &= 0, & (1)\\ \rho\partial_t\mathbf{V} + \mathbf{G}.\bar{\bar{\nabla}}\mathbf{V} + \bar{\bar{\nabla}}.(x(1-x)\rho\mathbf{V}_R\otimes\mathbf{V}_R) &= \rho\mathbf{g} - \boldsymbol{\nabla}P - \bar{\bar{\Lambda}}\mathbf{V} \\ &+ \bar{\bar{\nabla}}.\mu_T(\bar{\bar{\nabla}}\mathbf{V} + \bar{\bar{\nabla}}^T\mathbf{V}), & (2)\\ \rho\partial_t H + \mathbf{G}.\boldsymbol{\nabla}H + \boldsymbol{\nabla}.(x(1-x)\rho L\mathbf{V}_R) &= \boldsymbol{\nabla}.(\chi_T\boldsymbol{\nabla}H), & (3) \end{aligned}$$

with $\bar{\bar{\Lambda}}$ the singular-obstacle tensor and $\mathbf{V}_R$ the relative velocity given by the drift-flux Lellouche-Zolotar model [9] and based on the Zuber-Findlay approach [10]. The turbulent dynamic viscosity μ_T is given by the local scalar Schlichting model [11]:

$$\mu_T = a_S|\mathbf{G}|L_T \quad (4)$$

where L_T is a characteristic length and a_S a coefficient. The turbulent diffusion coefficient χ_T for the enthalpy balance equation is defined via the Prandtl number $P_r = \frac{\mu_T}{\chi_T}$. The density ρ, the static quality x and the latent heat L are determined through the equation of state of the water as a function of the pressure and mixture specific enthalpy. We solve in H, P and $\mathbf{V}$ variables. The time term presence in Eq. (2) allows to search the steady-state regime through a transient computation of a thermally dilatable fluid, $\boldsymbol{\nabla}.\mathbf{G} = 0$, cf.

Eq. (1). For that, the Chorin-Gresho method [12] (a fractional-step method) is used to solve the coupled mass-momentum equations. The non linearity are dealt by the Picard iterative process. The time discretization is based on a semi-implicit Crank-Nicholson scheme. The spatial discretization is based on the unstructured hexahedral finite elements (constant pressure by element and tri-linear velocity by node). The physical data ρ, μ_T and $\bar{\bar{\Lambda}}$ are constant by element. The Streamline Upwind Petrov-Galerkin method is applied to correct the convective term [13]. A conjugated gradient method, preconditioned by the diagonal, is used to solve the arising linear systems.
According to the hyperbolic nature of the flow equations, Dirichlet boundary conditions are used at the inlets of the domain (mass flux and enthalpy) and Neumann boundary conditions at the outlets (pressure). The other boundaries of the domain are impermeable walls. Generally, these are considered adiabatic and with no shear stress.

3 The Immersed Boundary Model

In the fictitious domain approach, introduced in the fifties by Hyman [14] and the Russian's school [3, 4], the original domain $\tilde{\Omega}$ is embedded in a fictitious domain Ω which is geometrically bigger and generally simpler-shaped. Doing this, some immersed boundary Σ appears such that $\Omega = \tilde{\Omega} \cup \Sigma \cup \Omega_e$, where Ω_e is the complementary or 'exterior' domain (as the fins). The spatial discretization is now performed in Ω, independently of the shape of the original domain $\tilde{\Omega}$. Then, the resolution of the new problem in Ω will be faster and simpler. The main issue is to enforce the original boundary conditions on the immersed interface Σ which is non-aligned with the mesh.

3.1 The ISI method

In this work, among the numerous fictitious domain methods (see [8] for a short introduction), we consider an element of the set of Immersed Boundary Methods: the fictitious domain method with Immersed Spread Interface (ISI) [15, 8]. The fictitious problem to be solved in Ω is built from the original problem in $\tilde{\Omega}$, but an additional term takes into account the immersed boundary conditions. For velocity Dirichlet boundary conditions, the singular-obstacle tensor $\bar{\bar{\Lambda}}$ of Eq. (2) will play this role. It allows us to take into account the no-penetration condition of the flow limiter fins in an implicit way during the first step of the Chorin-Gresho method.
Let us $(\mathbf{u}, \mathbf{v}, \mathbf{w})$ be the local basis linked to a given obstacle (i.e. fin). The vectors $\mathbf{u}$ and $\mathbf{v}$ are tangential to the obstacle and the vector $\mathbf{w}$ is normal to the obstacle. For the element e, we define the singular-obstacle tensor by:

$$\bar{\bar{\Lambda}}_e = \rho_e \frac{A_e}{\Omega_e} \begin{pmatrix} \Lambda_u & 0 & 0 \\ 0 & \Lambda_v & 0 \\ 0 & 0 & \Lambda_w \end{pmatrix} \tag{5}$$

with A_e the measure of this obstacle (area, m^2) intercepted by the element e and Ω_e the measure (volume; m^3) of this element. Λ_u, Λ_v and Λ_w are the tensor coefficients in, respectively, the directions $\mathbf{u}$, $\mathbf{v}$ and $\mathbf{w}$. Here, we consider no-penetration obstacles in

the normal direction, $\Lambda_w = 1/\epsilon$ with $0 < \epsilon << 1$, and slip conditions in the tangential directions, $\Lambda_u = \Lambda_v = 0$.
Immersed interfaces Σ, as the flow-limiter fins, are modeled by a collection of linear plane surfaces intercepting elements of Ω. In each intercepted element, the measure of the intercepted surface and the external normal vector are known. As the singular-obstacle tensor is defined by element, all the nodes belonging to this element are concerned: i.e. we have a spread interface approximation of Σ.

3.2 Convergence order and elements of validation

As for the L^2-penalty methods [3, 16], that the ISI method generalizes, the parameter ϵ is known as the penalty parameter. Regardless to the Navier-Stokes solving method, the theoretical rate of convergence of the penalized solution toward the body-fitted one is comprised in the range $[\mathcal{O}(\epsilon^{1/4}); \mathcal{O}(\epsilon^1)]$ in $L^2(\Omega)$ norm [16]. Let us notice that for Dirichlet boundary conditions and elliptic problems, the theoretical rate of convergence in space of the $\mathcal{Q}_1$-finite element method with non-boundary-fitted meshes is $\mathcal{O}(h^1)$ in $L^2(\Omega)$ norm, with h the space step [17].
As a whole, contributions to the validation of this IB approach can be found in [8] and [18]. On one side, in the context of dilatable two-phase flow elliptic problems, the work mentioned in [8] validates the ISI method with respect to body-fitted finite-element computations and to the JEBC method (an IB method using a finite-volume discretization). A first-order rate of convergence in space is numerically reached.

On the other side, in the context of incompressible one-phase flow Navier-Stokes equation, the work mentioned in [18] gives elements of validation for a finite-volume first-order penalty method very similar to the ISI method. Again, a first-order rate of convergence in space is numerically reached on the test case of a laminar flow around a static cylinder of diameter D (Reynolds number = 20). These results are in very good agreement with those proposed in the literature, cf. Table 1. In a lesser degree, it is also true for our own GENEPI results using the ISI method (about 10% on the drag coefficient and 30% on the recirculation length) giving confidence in the ability to catch the magnitude of an obstacle's drag coefficient.

Table 1: Hydrodynamic coefficients associated with the problem of steady flow around a static cylinder of diameter D (Reynolds number 20). B.F.: Body-fitted. C_d: drag coefficient. L_w: recirculation length. [18] (base) refers to the first-order penalty method of [18]. ISI: 18 cells in the diameter D and $\epsilon = 10^{-5}$.

	GENEPI		References [18]						
	B.F.	ISI	[18] (base)	Ye	Choi	Taira	Linnick	Fornberg	Tritton
C_d	2.13	2.30	2.06	2.03	2.02	2.06	2.06	2.00	2.09
$\frac{L_w}{D}$	0.96	1.22	0.93	0.92	0.9	0.94	0.93	0.91	-

4 CFD studies of the in-vessel flow limiter

This section is devoted to a first insight into the hydraulic of the in-vessel flow limiter through CFD simulations using the GENEPI code. We have set-up a preliminary design of the in-vessel flow limiter, cf. Fig. 3. In this preliminary work, we mainly restrict ourselves to liquid one-phase flows. But it is not a limitation; cf. [19] for illustrations of simulations with two-phase flows.
For simplicity reason, we do not give attention to the gravitational acceleration term in the computations (around the flow limiter, gravitational effects are negligible in comparison with the inertial ones during the fast-depressurization phase). As well, the pressure range considered here is only [40-60] bar. Concerning the turbulence model, cf. Eq (4), the GENEPI-code standard value for the Schlichting coefficient is $a_S = 0.047$ and the turbulence characteristic length L_T is related to the biggest eddy structures. As reference, we choose $L_T \approx 1\ m$ for the nominal-operation flow direction (azimuth scale in the down-comer) and $L_T \approx 0.3\ m$ for reverse flow direction toward the broken cold leg ($\approx$ radial scale in the down-comer).
As the GENEPI's turbulence model is quite rough, a parametric study is performed on the coefficient a_S and the turbulence characteristic length L_T, cf. Eq (4): $a_S \in \{$a=0.047, a/10$\}$ and $L_T \in \{0.3, 1.0, 2.0\}$. The value of the penalty parameter is set to $\epsilon = 10^{-5}$.
We consider that the GENEPI steady state is reached when the relative L^2-norm difference of the variables (pressure, mass flux and enthalpy) between two consecutive time iterations is less than $5.10^{-3}\delta t$ with δt the time step. Usually a CPU time of 5 to 6 hours is need to reach the steady state on the finest mesh M_3. It is compatible with a big number of simulations needed to optimize the flow limiter geometry.

4.1 Computational domain and meshing

The CFD computational domain Ω is a simplified rectangular geometry of 4.3 m x 4 m x 0.2 m to which was added the broken cold-leg nozzle starting about 1 m before the down-comer. It extends up to 2 m below the cold-leg axis. Considering a sectorized down-comer as in Fig. 1, we only model one third of the down-comer, including one cold-leg entry in the vessel and one hot-leg pipe, cf. Fig. 2. The measures of the computational domain volume, of the down-comer and the cold-leg nozzle surfaces are equal to 3.8 m^3, 0.9 m^2 and 0.4 m^2 respectively.
For the purpose of a mesh convergence study, three meshes M_1, M_2 and M_3 were built involving N_1 = 6,080, N_2 = 48,640 and N_3 = 164,160 elements respectively. The mean space step ranges from 0.2 m (M_1) to 0.07 m (M_3) and the ratio between two consecutive space-step indexes is 2.0 ($M_1 \to M_2$) and 1.5 ($M_2 \to M_3$).
The flow-limiter fins are modeled by singular-obstacle surfaces through a collection of plane surfaces, cf. Fig. 3.

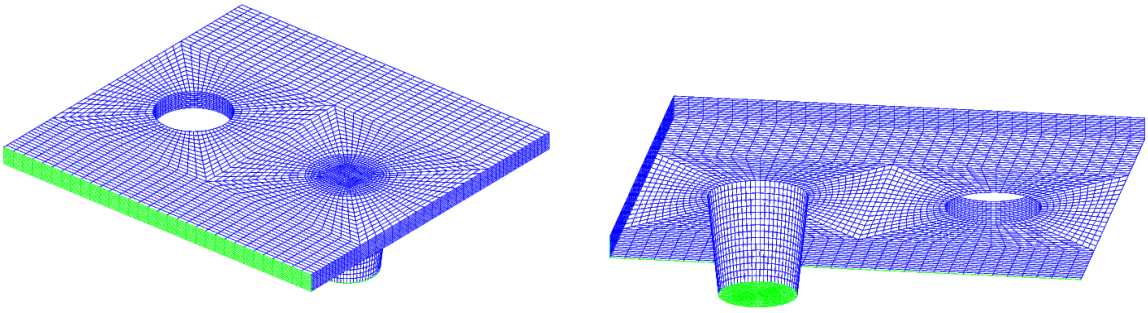

(a) Down-comer surface (green). (b) Cold-leg nozzle surface (green).

Figure 2: Example of the mesh used for the CFD study of the in-vessel flow limiter (mesh M_2; 48640 elements). The walls are colored in blue.

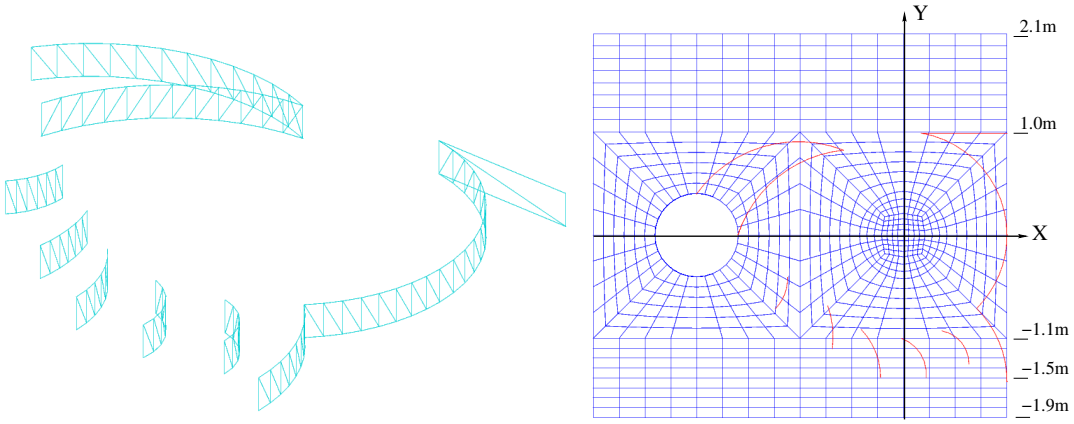

(a) Flow limiter meshing. (b) Singular obstacles positioned in the computational domain (mesh M_1; 6,080 elements).

Figure 3: Example of preliminary meshing of the flow limiter.

4.2 Boundary conditions

Slip-wall boundary conditions are considered on the walls, mass flux Q_{in} is imposed on the in-flow boundary and *ad-hoc* pressure $P_{out} = 50$ bar on the out-flow boundary. The in-flow and out-flow surfaces are the down-comer and the cold-leg nozzle surfaces depending on the considered main-flow direction. The inlet mass-flux values are $Q_{in} =$ 4,690 kg/s in nominal-operation condition (default flow direction; in $\leftrightarrow$ cold leg and out $\leftrightarrow$ downcomer) and $Q_{in}=$ 5,200 kg/s in LB-LOCA condition (reverse flow direction; in $\leftrightarrow$ downcomer and out $\leftrightarrow$ cold leg).

4.3 Results

All quantitative results concerning the pressure-drop coefficients for the various turbulence-model coefficients and meshes are grouped in Tab. 2. In this table, the bold-typed turbulence parameters are the reference ones. Also the global pressure-drop coefficients

computed by GENEPI, with or without in-vessel flow limiter, on the finest mesh M_3 are bold-typed. These can be compared to the global pressure-drop coefficients found in literature (Borda-Carnot law or Idel'cik). Although the mesh convergence is not fully reached, the trend of the evolution of the pressure-drop coefficient versus the space-step index is globally caught.

Figs 4 to 6 present some field distributions concerning the mixture velocity, the mixture

Table 2: Summary of the global pressure-drop coefficients K_{gl}. The default flow direction is defined as the nominal-operation flow direction (from the cold leg to the down-comer). The reverse flow direction is defined as the opposite direction. (*): unsteady computation.

		Without limiter			With limiter		
Flow direction	Turbulence	K_{M1}	K_{M2}	K_{M3}	K_{M1}	K_{M2}	K_{M3}
Default	a; L_T=2 m	2.5					
	a/10; L_T=2 m	0.4					
	a/10; L_T=0.3 m	$0.4^{(*)}$					
	a; L_T=0.3 m	0.4	0.3	**-0.3**	6.2	$1.8^{(*)}$	$\mathbf{0.7}^{(*)}$
	a; L_T=1.0 m	1.2	0.8	**0.1**	9.8	$3.1^{(*)}$	**1.6**
Idel'cik [20]		$K_{gl} \approx +0.5$					
Borda-Carnot ($\xi = 1$)		$K_{gl} \approx$ -0.5					
Reverse	a; L_T=2 m	4.6	4.2				
	a/10; L_T=2 m	$4.7^{(*)}$	$4.2^{(*)}$				
	a; L_T=0.3 m	$4.3^{(*)}$	$2.7^{(*)}$	**3.6**	13.3	5.3	**5.4**
	a; L_T=1.0 m	3.9	3.7	**3.7**	15.9	7.0	**6.4**
Idel'cik [20]		$K_{gl} \approx 1.2$					
Borda-Carnot ($\xi = 1$)		$K_{gl} \approx 1.1$					

pressure and the local external forces taking into account the flow-limiter fins $\bar{\bar{\Lambda}}\mathbf{V}$, cf. Eq. (2) for the two studied flow configurations (nominal condition and reverse condition). For the nominal-operation configuration (fluid flowing toward the down-comer), the pressure and velocity distributions are shown in Figs 4(a) and 5(a). The local external-force distribution is illustrated in Fig. 6(a). The introduction of the flow-limiter device induces an irregular flow path with the emergence of flow channels between the fins. Also, the in/out-flow pressure difference is increased in reference to the case without in-vessel flow limiter: $K_{M3} \in [-0.3; +0.1] \rightarrow [0.7; 1.6]$, cf.Table 2. Let us notice that, without flow limiter, the range of CF-computed values $K_{M3} \in [-0.3; +0.1]$ is compatible with the Idel'cik (output of a rectilinear diffuser on a screen) or Borda-Carnot (sudden flow-section expansion) estimation one $K_{gl} \in [-0.5; +0.5]$.

For the reverse-flow configuration (fluid flowing toward the broken cold leg), the pressure and velocity distributions are shown in Figs 4(b) and 5(b). The local external-force distribution is illustrated in Fig. 6(b). The introduction of the flow-limiter device clearly increases the fluid vortex at the entry of the broken cold leg and the in/out-flow pressure drop. The global pressure-drop coefficient is multiplied by almost a factor two in case of flow limiter: $K_{M3} \in [3.6; 3.7] \rightarrow [5.4; 6.4]$, cf. Table 2. Obviously the geometry of the fins

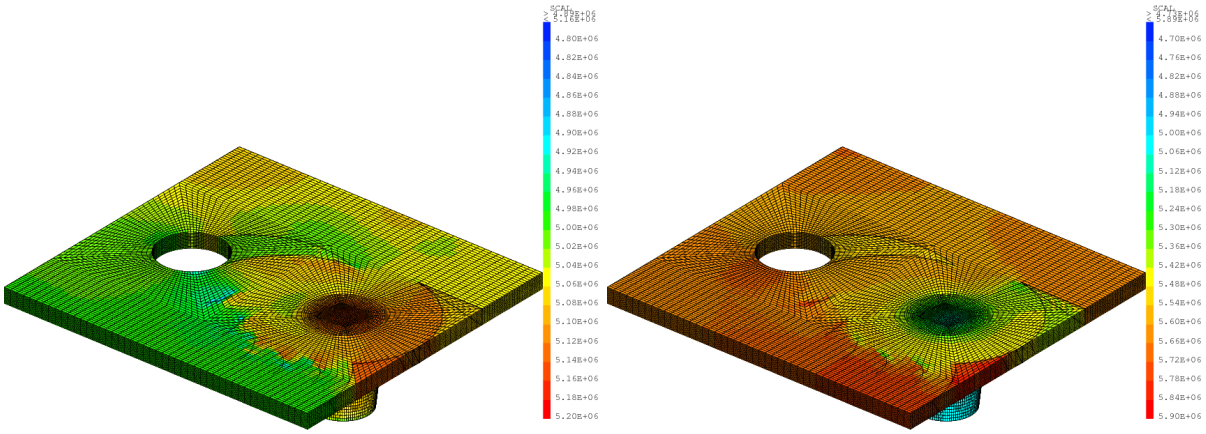

(a) Nominal-operation condition (b) LB-LOCA condition

Figure 4: Pressure; mesh M_3 (164,160 elements); ($a_S = a; L_T = 0.3\ m$). Pressure iso-values ranges from 4.8 to 5.2 bar.

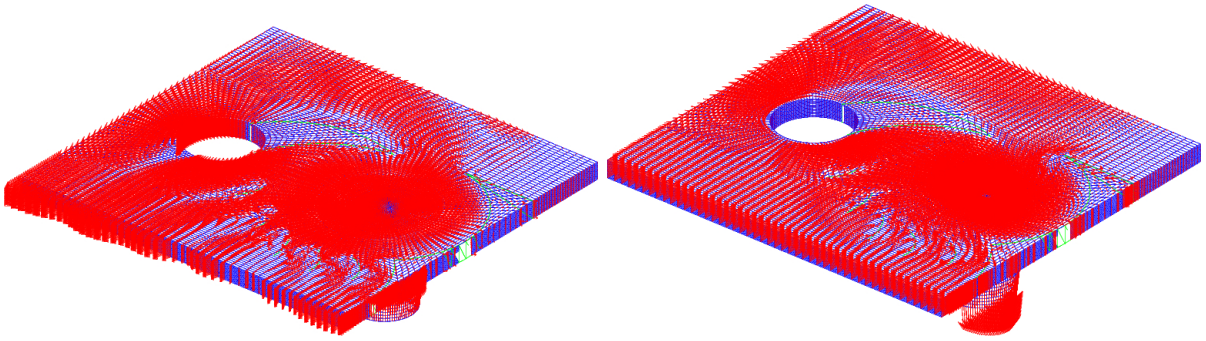

(a) Nominal-operation condition (b) LB-LOCA condition

Figure 5: Velocity; mesh M_3 (164,160 elements); ($a_S = a; L_T = 0.3\ m$).

has to be optimized to enhance this effect while limiting the flow-limiter impact during nominal operations.
Contrary to the nominal-operation case, the range of CF-computed values without flow limiter $K_{M3} \in [3.6; 3.7]$ sensibly differs from the Idel'cik (conical collector with front wall and screen) or Borda-Carnot (sudden flow-section reduction) estimation one $K_{gl} \in [1.1; 1.2]$. But the hydraulic path is quite complex and does not reduce to simple configurations.

Finally, considering Fig. 6, we conjuncture that the impact on the flow of the fins located at the bottom of the flow limiter is much greater during LB-LOCA condition than during nominal-operation one.

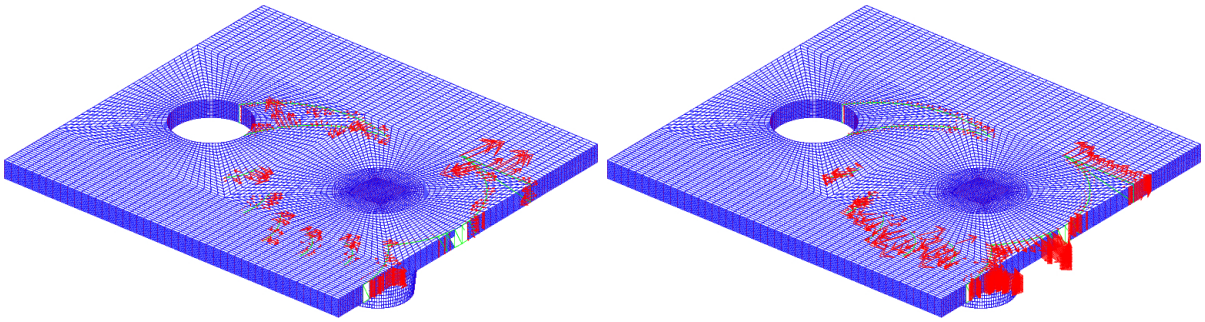

(a) Nominal-operation flow; ($a_S = a; L_T = 0.3\ m$). (b) Reverse flow; ($a_S = a; L_T = 1.0\ m$).

Figure 6: Local external-force distribution; mesh M_3 (164,160 elements).

5 Conclusions and perspectives

In this paper, we have presented a CFD model of an in-vessel flow limiter to mitigate the consequences of a large-break loss of coolant accident in a pressurized-water reactor. The principle of this safety device is based on fins designed to create a strong flow vortex increasing the pressure drop toward the broken cold leg. A *rough* CFD model using a homogeneous relaxed equilibrium model of a liquid-vapour mixture and an immersed boundary approach has been set-up, allowing a less precise but fast estimation of the pressure drop following the geometry of the fins. Through 3D/1D up-scaling of a global pressure-drop coefficient, local pressure-drop coefficients can be provided to thermal-hydraulic system safety codes, allowing the study of the in-vessel flow limiter effect on the thermal-hydraulic system.
One-phase fluid CFD simulations have been run using the GENEPI code with a computation domain defined in coherence with the downcomer of a PWR. Parametric studies on the turbulence model lead to determine the range of the global pressure-drop coefficients depending on the direction of the flow and the presence of the flow limiter, opening the way to take into account the in-vessel flow limiter in a realistic manner. Nevertheless, considering the limitations related to the turbulence model, this conclusion needs to be consolidated by body-fitted CFD studies with more precise turbulence models.
Some perspectives can be outlined about the improvement of this numerical model in order to proceed to the geometry optimization of the design of the flow-limiter fins. In particular, we can mentioned the space-interpolation scheme across the boundary interface to reach the second order [18] and the definition of immersed-wall laws for RANS/large-eddy simulations.

REFERENCES

[1] Advanced Reactors Information System (ARIS). International Atomic Energy Agency, *https://aris.iaea.org/sites/overview.html*.

[2] Gautier, G.-M. Dispositif limiteur de débit inverse de fluide (in French). *Patent n°***88 12665**, 1988.

[3] Saul'ev, V. On the solution of some boundary value problems on high performance computers by fictitious domain method (in Russian). *Siberian Math. Journal* (1963) **4(4)**:912–925.

[4] Rukhovets, L. A remark on the method of fictive domains (in Russian). *Differential Equations* (1967) **3(4)**:114–121.

[5] Clerc, S. Numerical simulation of the Homogeneous Equilibrium Model for two-phase flows. *Journal of Computational Physics* (2000) **161(1)**:354–375.

[6] Grandotto, M. and Obry, P. Calculs des écoulements diphasiques dans les échangeurs par une méthode aux éléments finis (in French). *Revue Européenne des Eléments Finis* (1996) **5(1)**:53–74.

[7] Grandotto, M. and Obry, P. Steam generator two-phase-flow numerical simulation with liquid and gas momentum equations. *Nuclear Science and Engineering* (2005) **151**:313–318.

[8] Belliard, M. and Ramière, I. Fictitious domain methods for two-phase flow energy balance computations in nuclear components. *International Journal for Numerical Methods in Fluids* (2012) **68(8)**:939–957.

[9] Lellouche, G. S. and Zolotar, B. A. Mechanistic model for predicting two-phase void fraction for water in vertical tubes, channels and rod bundles. *Special Report, EPRI* (1982) **NP 2246-SR**.

[10] Zuber, N. and Findlay, J. Average volumetric concentration in two-phase flow systems. *J. Heat Transfer* (1965) **87(4)**:453–468.

[11] Schlichting, H. *Boundary layer theory*. Mac Graw Hill, New York, USA, 1968.

[12] Gresho, P. and Chan, S. On the theory of semi implicit projection methods for viscous incompressible flow and its implementation via finite element method that also introduces a nearly consistent matrix. i, theory. *International Journal for Numerical Methods in Fluids* (1990) **11(5)** 587–620.

[13] Brooks, A. and Hughes, T.-R. Streamline upwind/Petrov-Galerkin formulations for convection dominated flows with particular emphasis on the incompressible Navier-Stokes equations. *Computer methods in Applied Mechanics and Engineering* (1982) **32(1-3)** 199–259.

[14] Hyman, M. Non-iterative numerical solution of boundary-value problems. *Applied Scientific Research, Section B* (1952) **2(1)**:325–351.

[15] Ramière, I. and Angot, P. and Belliard, M. A fictitious domain approach with spread interface for elliptic problems with general boundary conditions. *Computer Methods in Applied Mechanics and Engineering* (2007) **196(4-6)**:766–781.

[16] Angot, P. and Bruneau, C.-H. and Fabrie, P. A penalization method to take into account obstacles in incompressible viscous flows. *Numerische Mathematik* (1999) **81(4)**:497–520.

[17] Ramière, I. Convergence analysis of the Q1-finite element method for elliptic problems with non-boundary-fitted meshes. *International Journal for Numerical Methods in Engineering* (2008) **75(9)**:1007–1052.

[18] Introïni, C. and Belliard, M. and Fournier, C. A second order Penalized Direct Forcing for hybrid Cartesian/Immersed Boundary flow simulations. *Computers & Fluids* (2014) *90*:21–41.

[19] Belliard, M. Numerical modeling of an in-vessel flow limiter using an Immersed Boundary Approach. *Nuclear Engineering and Design* (2014) **90**:21–41.

[20] Idel'cik, I. *Mémento des pertes de charge* (in French). 1999th Edition, Collection de la Direction des Etudes et Recherches d'Electricité de France, Eyrolles, 1960.